

SPECTRAL LINES FOR POLARIZATION MEASUREMENTS OF THE CORONAL MAGNETIC FIELD. I. THEORETICAL INTENSITIES

P. G. JUDGE

High Altitude Observatory, National Center for Atmospheric Research,¹ P.O. Box 3000, Boulder, CO 80307-3000

Received 1997 November 10; accepted 1998 April 10

ABSTRACT

Infrared emission lines are potentially sensitive probes of components of the coronal vector magnetic field, through the Zeeman effect, and on its direction projected onto the plane of the sky, through fluorescent polarization of scattered photospheric light. Prompted by the advent of sensitive infrared array detectors, existing atomic data were reexamined to compile a complete list of coronal lines that may yield a detectable Zeeman effect, through careful differential measurements of Stokes profiles, at typical coronal field strengths of order 10 G. “Average” intensities were computed for a subset of promising forbidden coronal lines. A representative coronal density structure was used. The distribution of plasma with temperature was, at all heights in the corona, assumed to be that described by a standard differential emission measure from extreme-ultraviolet observations of the solar disk. Effects of excitation by photospheric radiation were included, as well as cascades from collisionally excited higher levels having the same principal quantum number as the ground levels. The largest source of error in the computed intensities lies in the form assumed for the emission measure distribution. The assumed density and temperature structure is too simple for detailed comparisons with observations of a particular coronal structure. Nevertheless, existing observed intensities are consistent with the calculations, which suggests that the theoretical intensities of (as yet) unobserved lines can be used as a basis for further study. The strongest predicted lines arise from magnetic dipole transitions within the ground terms of the $2s^m 2p^n$ and $3s^m 3p^n$, $m = 1, 2$, $n = 1, \dots, 5$, configurations. The most promising lines lie between 1 and 10 μm , the lower limit being set by the need to detect small field strengths. The upper limit is set by the small Einstein A -coefficients and the smaller intensities of the exciting photospheric light, both of which lead to smaller forbidden line intensities. The most promising lines include [Fe XIII] 1.0747, 1.0798 μm ; [Si X] 1.43 μm ; [Si IX] 2.58, 3.93 μm ; [Mg VIII] 3.03 μm ; and [Mg VII] 5.50, 9.03 μm . An aircraft experiment is being prepared to obtain targeted portions of the coronal spectrum between 1 and 10 μm during the 1998 February 26 eclipse, with the goal of detecting some of these promising lines. This work will help toward the planning and development of efficient magnetographs, perhaps space-borne, for the routine measurement of coronal magnetic fields in the quiet and active Sun.

Subject headings: polarization — Sun: atmosphere — Sun: corona — Sun: infrared —
Sun: magnetic fields

1. INTRODUCTION

The evidence for magnetic control of the Sun’s corona is overwhelming, from early eclipse and coronagraphic observations showing loop structures to present-day images from the *Yohkoh* satellite and *SOHO* spacecraft. It is abundantly clear, from observations of the 10^6 K coronal plasma, that the magnetic fields emerging from beneath the Sun’s photosphere control essentially all aspects of coronal structure and dynamics, from plasma-heating mechanisms through to coronal evolution on the largest spatial scales (for reviews, see Bray et al. 1991; Low 1994; Golub & Pasachoff 1997).

Unfortunately, it is equally clear that our empirical knowledge of the controlling coronal magnetic fields is extremely limited. Direct determinations of coronal magnetic fields in the “ordinary” corona (i.e., the 10^6 K plasma in the quiet Sun or surrounding active regions) are limited to regions 100 R_\odot or more above the photosphere where spacecraft can operate (e.g., Erdos, Balogh, & Kota 1997; Forsyth et al. 1997). In such regions, the plasma β is of order 1 or more, i.e., the energy density is dominated by plasma motions and the field lines have already been “opened” by

the solar wind outflow. Such measurements contain little, if any, useful information about conditions in the inner corona, beyond the statement that the magnitude of the field at 1 AU implies average field strengths close to 10 G at the coronal base.

Remotely sensed determinations of coronal magnetic fields have been limited to special regions of the solar atmosphere and/or at special times. Radio observations of unusually strong field regions (greater than 100 G) overlying active regions can yield information on projections of the vector magnetic field B through the gyroresonance mechanism. A substantial literature has evolved on this subject since gyroresonance emission was predicted by Ginzburg & Zheleznyakov (1961) (and in earlier papers in Russian). The mechanism was confirmed through various studies, based on comparisons between extreme-ultraviolet (EUV) observations with *Skylab* and radio aperture synthesis work (e.g., Kundu, Schmahl, & Gerassimenko 1980; Pallavicini, Sakuri, & Vaiana 1981; Webb et al. 1983; Shibasaki et al. 1983), on the appearance of “ring” structures and characteristic polarization signals in radio data (Alissandrakis & Kundu 1982; Lang & Willson 1982) predicted in the presence of gyroresonance opacity by Gelfreikh & Lubyshev (1979), and on the detection of individual “lines” in the gyroresonant spectrum (Willson 1985).

¹ The National Center for Atmospheric Research is sponsored by the National Science Foundation.

Recent papers have developed this area to the extent that "coronal magnetography" of active regions using this method is entering a phase of maturity (e.g., White, Kundu, & Gopalswamy 1991; Gary & Hurford 1994; Schmelz et al. 1994; Brosius et al. 1997), with the higher spatial resolution and spectral coverage possible today.

As for active regions, prominences must also be considered a special case, in which specific thermal conditions exist that permit application of the Hanle effect and the Zeeman effect in ions of unusually low ionization degree (see Koutchmy's 1995 review, for example). Magnetic field determinations can also be made by Faraday rotation measurements of cosmic radio sources (e.g., Gelfreikh 1994). In all of these cases, the regions of the corona that can be measured are "special," being specific locations determined by special thermodynamic conditions, by special magnetic configurations, or by particular lines of sight through the corona.

In the 10^6 K, low- β coronal plasma typically found in the quiet Sun, there are only very weak signatures of the presence of the magnetic field in the emitted spectra. For instance, thermal bremsstrahlung can be used to determine longitudinal magnetic field strengths through observations of left and right circularly polarized radio waves. These observations are difficult owing to the extremely high sensitivity needed, and results are quite scarce (e.g., Gelfreikh 1994).

Currently, our view of the vector field in the 10^6 K corona of the quiet Sun in fact comes almost entirely from extrapolation of photospheric magnetic field measurements. While significant efforts have been made to determine the morphology of the inferred coronal magnetic fields through comparisons of calculations with active region EUV plasma loops in active regions (e.g., Schmieder et al. 1996), such extrapolations are inherently limited by theoretical uncertainty in the models used owing to the ill-posed nature of the problem (e.g., Low & Lou 1990). In the quiet Sun, the problem is considerably worse owing to the weaker, less ordered fields there. Experimental determinations of the magnetic field, B , in the 10^6 K corona are needed to put coronal physics on a firm empirical foundation. Such measurements are needed to address many crucial questions: How reliable are extrapolations that are commonly used today? Do the fields carry large-scale currents, and how are these currents formed (e.g., Leka et al. 1996)? How complex or "braided" is the field within a given loop, and how does this influence models of coronal heating (e.g., Parker 1988)? What kind of field configurations lead to prominence formation (Low & Hundhausen 1995)? What causes the dynamic behavior seen in flares and coronal mass ejections (e.g., Low 1994)?

Two diagnostics of the 10^6 K coronal plasma's magnetic field exist that have not yet been proven useful: the Hanle effect, for which the Ly α line of hydrogen holds the most promise (e.g., Fineschi et al. 1993), and the Zeeman effect. The first method suffers from the disadvantage that at present there is no complete quantum theory to attack the general problem of the frequency-dependent resonance scattering process including quantum coherences between sublevels. Nevertheless, a recent heuristic extension of the standard theory by Landi Degl'Innocenti et al. (1996) is promising (Landi Degl'Innocenti 1998).

The purpose of the present paper is to identify, through theoretical calculations, a set of infrared forbidden coronal

emission lines that can be expected to reveal properties of the 10^6 K coronal plasma's magnetic field of the quiet Sun using Stokes polarimetry, through the Zeeman effect. The line profiles, which are observable not on the disk but above the solar limb, in principle contain information on the vector magnetic field through small but systematic line shifts between the different polarization states arising from the Zeeman effect, which can be determined through careful differential measurement techniques (Kuhn 1995). This paper is devoted only to the calculation of intensities, comparisons with observations, identification of excitation mechanisms, and a first assessment of the best emission lines that promise to be useful. Later work will focus upon simulation of the full Stokes vectors, including the effects of the Earth's atmosphere and instrumental properties, in order to identify the best lines, the kind of instrumentation needed for future measurement efforts, and problems concerning inversion of the polarization data to derive magnetic fields. It is hoped that such lines may eventually yield magnetic field determinations that are complementary to the more established radio techniques, yielding information on larger volumes of the corona and in weaker field regions.

This paper is organized as follows. First, a brief review is given of previous attempts to measure coronal field strengths, of the techniques that are available, and of the potential advantages offered by selecting infrared transitions. Next, since previous work lacks completeness in terms of atomic data and treatment of excitation processes, detailed calculations are presented for specific ions that are likely to be of interest, based upon a complete survey of interesting atomic transitions discussed in the Appendix. Finally, comparisons with observations are made, and a list of potentially useful lines is compiled.

2. EMISSION LINES AS DIAGNOSTICS OF CORONAL MAGNETIC FIELDS

Extrapolations of fields measured at 1 AU indicate field strengths of order 10 G in the quiet Sun's corona. Such estimates immediately reveal the well-known reason that direct measurements of 10^6 K coronal plasma fields have so far eluded observers. Fields of this magnitude are notoriously difficult to measure from properties of radiation emitted in 10^6 K plasmas (e.g., Harvey 1969). To see why, we note that of those techniques that can be presently applied to 10^6 K plasmas, there are just *three* that are potentially useful:

1. The Hanle effect can be used in permitted lines, especially H Ly α .
2. The Zeeman effect can in principle be used to determine line-of-sight projections of the vector magnetic field, using differential measurements in circularly polarized light.
3. Linear polarization degree measurements for certain forbidden coronal lines that are excited by the anisotropic photospheric radiation can constrain the direction of the magnetic field in the plane of the sky (POS). This will be referred to henceforth as the "fluorescent polarization" method.

The Hanle effect will not be discussed further. The Zeeman effect produces Stokes profiles that are in the (very) weak field limit. Doppler widths exceed the wavelength shifts seen in different Stokes parameters by several orders of magnitude. The Doppler width of [Fe XIII] 10747 Å, for example, is 3 orders of magnitude larger than the wave-

length shifts induced in different states of circular polarization by a 10 G field component along the line of sight (LOS). Thus, careful measurements differential in wavelength as well as polarization state are required (see Kuhn 1995) with high signal-to-noise ratios. Using circular polarization measurements, Harvey (1969) derived upper limits of several tens of gauss for the LOS component ($|B_{\parallel}|$) from observations of the green line [Fe xiv] 5304 Å. Similarly, an upper limit of 40 G was determined by Kuhn (1995) using [Fe xiii] 10747 Å line profiles observed with a 0.4 m coronagraph outside of eclipse.

The fluorescent polarization method has been successfully applied to observations of the [Fe xiii] 10747 Å line (e.g., Arnaud & Newkirk 1987 and references therein). The method relies on the fact that certain radiatively excited transitions originate in resonant transitions between radiatively “aligned” Zeeman substates (e.g., Sahal-Bréchet 1977). It does not require wavelength resolution across line profiles, and it has intrinsically high fractional polarizations (several tens of percent are possible; e.g., see Sahal-Bréchet 1977). Thus, these measurements are easier to make than those needed for the Zeeman effect. A necessary (but not sufficient) condition for the fluorescent polarization method to work is that the line is excited, at least in part, by the absorption of the anisotropic photospheric radiation. If the excitation mechanism for a given line satisfies a sufficiency condition (see Sahal-Bréchet 1977 for the particular case of [Fe xiii]), then both methods can be applied simultaneously to coronal forbidden lines.

In summary, although measurements have been made that have constrained the direction of coronal magnetic fields in the POS, to date no magnetic field strength measurements have been made in the quiet Sun’s corona, owing to difficulties in measuring small differential properties of Stokes profiles. The work of Kuhn (1995) is an important first step along the path for developing coronal magnetometry beyond its modest beginning in the 1960s and 1970s. His upper limit of 40 G, which was obtained with a coronagraphic instrument using a good, but not state-of-the-art, detector, is close to expected field strengths. He emphasized that the infrared (IR) spectral region can offer significant advantages over optical wavelengths. In particular, the sensitivity of Doppler-broadened Stokes profiles to the Zeeman effect increases linearly with the wavelength of the line. Recent improvements in the sensitivity and size of IR detector arrays also open up the possibility for very sensitive measurements over large projected volumes of the corona.

3. CALCULATIONS OF THE INFRARED LINE SPECTRUM OF THE CORONA

3.1. *The Need for Theoretical Spectral Calculations*

Our knowledge of the IR spectrum of the Sun’s corona is surprisingly sparse. Only seven or so lines have been identified in the IR region between 1 and 3 μm (Olsen, Anderson, & Stewart 1971; Kastner 1993; Kuhn 1995). This stands in contrast to the large number of lines expected in this wavelength range and at longer wavelengths from compilations of atomic energy level data of highly ionized ions (Edlén 1943; Rohrllich & Pecker 1963; Pryce 1964; Collins 1964; Kaufman & Sugar 1986). This is due to the relative weakness of the coronal forbidden lines compared with the solar disk brightness, to the difficulties in measuring IR lines

under high, varying spectral background conditions, and to the restricted windows in the atmospheric transmission of IR radiation.

This situation motivates the use of theoretical calculations to explore and identify strong IR forbidden coronal lines. However, calculations needed to compute a synthetic coronal spectrum are generally unavailable. With interest in data from the recently launched *Infrared Space Observatory* satellite, Greenhouse et al. (1993) computed the properties of a set of ions under conditions believed to be present in the line-emitting regions of Seyfert galaxies. While aspects of these calculations will be used below, their usefulness is limited by the omission of two processes known to be important in the formation of some forbidden lines in the corona: photoexcitation by the anisotropic solar photospheric field and cascades from higher atomic levels excited by electron collisions (e.g., Flower & Pineau des Forêts 1973; Sahal-Bréchet 1974). Both are crucial processes to model correctly because not only are intensities greatly influenced, but the fluorescent polarization method relies primarily on photoexcitation as a significant excitation process. Calculations are therefore needed (1) to determine which types of lines in which kinds of elements and ions are expected to be strongest and (2) to perform detailed calculations for specific cases, including all processes known to be important, to produce synthetic forbidden line spectra of the corona.

3.2. *First Calculations*

Before embarking on detailed calculations, it is appropriate (and necessary) to review and refine a large list of potentially interesting transitions (Kaufman & Sugar 1986). In the Appendix, a “first pass” through atomic data is described. The survivors of this first cut, based on abundances listed in Table 1 and drawing heavily on the work of Greenhouse et al. (1993), are listed in Table 2. These are potentially bright (mostly IR) lines arising from transitions within the $2s^m 2p^n$ and $3s^m 3p^n$, $m = 1, 2, n = 1, \dots, 5$ configurations in abundant ions. All other transitions are likely to be substantially weaker on the basis of small branching

TABLE 1
ADOPTED ABUNDANCES

Element	\log_{10} Abundance
Ne	8.09
Na	6.78
Mg	8.03
Al	6.92
Si	8.00
S	7.21
Ar	6.56
Ca	6.81
Cr	6.12
Fe	8.12
Ni	6.70

NOTE.—Coronal abundances, adapted from photospheric abundances from Grevesse & Anders (1991). The values are those listed by Grevesse & Anders, with 0.45 added for elements with ionization potentials below 9 eV. The numbers given are on the scale where hydrogen has a logarithmic abundance of 12.

TABLE 2
POTENTIALLY INTERESTING LINE LIST

Sequence	Transition	Ion	λ (μm)	Relative $\xi(T) \cdot n_{\text{EL}}/n_{\text{H}}$ (Normalized to Fe XIV)		
Be	$^3P_2^o \rightarrow ^3P_1^o$	Na VIII	6.225	0.004		
		Mg IX	4.064	0.204		
		Al X	2.753	0.029		
		Si XI	1.904	0.550		
		S XIII	1.030	0.112		
B	$^2P_{3/2}^o \rightarrow ^2P_{1/2}^o$	Ne VI	7.631	0.027		
		Na VII	4.674	0.003		
		Mg VIII	3.028	0.076		
		Al IX	2.044	0.016		
		Si X	1.430	0.347		
		S XII	0.7611	0.089		
		Ar XIV	0.4411	0.028		
C	$^3P_1 \rightarrow ^3P_0$	Mg VII	9.031	0.047		
		Al VIII	5.846	0.006		
		Si IX	3.928	0.191		
		S XI	1.920	0.089		
		Ar XIII	1.018	0.025		
		Ca XV	0.5694	0.049		
		$^3P_2 \rightarrow ^3P_1$	Mg VII	5.502	0.047	
			Al VIII	3.689	0.006	
			Si IX	2.584	0.191	
			S XI	1.392	0.089	
	Ar XIII		0.8360	0.025		
	N	$^2D_{5/2}^o \rightarrow ^2D_{3/2}^o$	Ca XV	0.5444	0.049	
			S X	8.674	0.056	
			Ar XII	3.004	0.020	
			Ca XIV	1.307	0.049	
Ca XIV			0.9122	0.049		
O			$^2P_{3/2}^o \rightarrow ^2P_{1/2}^o$	Mg V	5.607	0.018
				Al VI	3.659	0.002
	Si VII	2.481		0.044		
	S IX	1.252		0.031		
	Ar XI	0.6929		0.020		
	Ca XIII	0.4087		0.045		
	$^3P_1 \rightarrow ^3P_2$	Mg V		13.53	0.018	
		Al VI		9.113	0.002	
		Si VII		6.513	0.044	
		S IX		3.754	0.031	
		Ar XI	2.617	0.020		
	F	$^2P_{1/2}^o \rightarrow ^2P_{3/2}^o$	Ca XIII	2.258	0.045	
			Al V	2.905	0.001	
			Si VI	1.964	0.022	
			S VIII	0.9913	0.012	
Ar X			0.5534	0.036		
Ca XII			0.3328	0.036		
S V			13.13	0.003		
Mg	$^3P_2 \rightarrow ^3P_1$	Ar VII	5.951	0.002		
		Ca IX	3.088	0.012		
		Cr XIII	1.088	0.009		
		Fe XV	0.7347	1.000		
		Ar VI	4.544	0.001		
Al	$^2P_{3/2}^o \rightarrow ^2P_{1/2}^o$	Ca VIII	2.321	0.005		
		Cr XII	0.8153	0.007		
		Fe XIV	0.5303	1.000		
		Ca VII	6.153	0.003		
		Cr XI	1.806	0.007		
Si	$^3P_1 \rightarrow ^3P_0$	Fe XIII	1.0747	0.912		
		Ni XV	0.6702	0.038		
		Ca VII	4.086	0.003		
		Cr XI	1.551	0.007		
		Fe XIII	1.0798	0.912		
	$^3P_2 \rightarrow ^3P_1$	Ni XV	0.8024	0.038		
		Cr X	4.260	0.005		
		Fe XII	2.217	0.724		
		Ni XIV	1.282	0.038		
		Ca VI	17.98	0.001		
P	$^2D_{5/2}^o \rightarrow ^2D_{3/2}^o$	Cr X	3.103	0.005		
		Fe XII	1.561	0.724		
		Ni XIV	0.8691	0.038		
		Ca V	4.157	0.001		
		Cr IX	1.278	0.003		
S	$^3P_1 \rightarrow ^3P_2$	Fe XI	0.7892	0.724		

TABLE 2—Continued

Sequence	Transition	Ion	λ (μm)	Relative $\xi(T) \cdot n_{\text{EL}}/n_{\text{H}}$ (Normalized to Fe XIV)
	$^3P_0 \rightarrow ^3P_1$	Ni XIII	0.5116	0.035
		Ca V	11.48	0.001
		Cr IX	5.786	0.003
		Fe XI	6.098	0.724
		Ni XIII	19.29	0.035
Cl	$^2P_{1/2}^o \rightarrow ^2P_{3/2}^o$	Cr VIII	1.010	0.001
		Fe X	0.6374	0.457
		Ni XII	0.4231	0.027
Ar	$^3P_2 \rightarrow ^3P_1$	Fe IX	1.867	0.457
		Ni XI	1.279	0.027
	$^3F_3 \rightarrow ^3F_4$	Fe IX	2.855	0.457
		Ni XI	2.571	0.027
		Fe IX	2.218	0.457

NOTE.—The last column lists the order of magnitude estimate of the leading terms determining the line intensity, the product of the abundance of the element and the relative differential emission measure at a temperature $T = 10^4(z + 1)^2$ K, where z is the charge on the ion. These quantities are normalized such that lines of Fe XIV have the value unity (see text). Wavelengths, which are from the NIST on-line database, are generally accurate to one part in 10^3 (see the Appendix).

ratios, high probabilities for photon collisional destruction, and/or abundances, and they can be neglected. Two exceptions ([Fe XI] and [Ni XIII]) were included in the list because of an interesting anomaly leading to very long wavelengths for a particular transition (see the Appendix).

3.3. Intensity Calculations

3.3.1. Basic Equations

Ignoring stimulated emission, background sources of emission, and other sources of emission along the LOS, the frequency-integrated intensity of an optically thin line centered at rest wavelength λ_k is given by

$$I_k = \frac{hc}{\lambda_k} \frac{1}{4\pi} \int_{-\infty}^0 n_{j(k)}(s) A_k ds \text{ ergs cm}^{-2} \text{ s}^{-1} \text{ sr}^{-1}, \quad (1)$$

where the symbols h and c have their usual meanings, A_k is the Einstein A -coefficient of the line labeled k , and $n_{j(k)}(s)$ is the population density of the upper level $j(k)$ of line k at position s along the LOS. The integration extends along the LOS. Assuming that the plasma does not evolve rapidly with time, the population densities are determined from rate equations of the form [the label (k) is dropped henceforth]

$$\sum_{j \neq i} n_j(s) P_{ji}(s) - n_i(s) \sum_{j \neq i} P_{ij}(s) = 0 \quad (2)$$

and the particle conservation equation

$$\sum_i n_i(s) = \frac{n_{\text{el}}(s)}{n_{\text{H}}(s)} n_{\text{H}}(s), \quad (3)$$

where $n_{\text{H}}(s)$ is the number density of hydrogen nuclei and $n_{\text{el}}(s)/n_{\text{H}}(s)$ is the abundance of the element relative to hydrogen. In equation (2), $P_{ji}(s)$ is the total (collisional plus radiative) transition probability, in units of s^{-1} , at which an ion in level j makes a transition to level i .

For the lines considered in Table 2, collisions between the ions of interest and electrons and protons only need be considered. Photospheric radiation must also be included because it irradiates the corona, and the excitation prob-

abilities can be comparable to or larger than collisional probabilities for certain optical and infrared transitions.

3.3.2. Ray Integrations and Temperature Distributions

Given a thermal model of the corona specifying electron and proton densities and temperatures as a function of radius (spherical symmetry is assumed here) and element abundances and given the photospheric radiation field and transition probabilities, it is straightforward to solve numerically equations (2) and (3) and derive intensities through equation (1). Such calculations suffer, however, from a serious shortcoming. The LOS in the real Sun intersects plasmas at a wider variety of different temperatures than can be accounted for in any reasonable model assuming spherical symmetry. Model calculations, in which temperature is specified only as a function of radius, cannot reproduce adequately the distribution of material as a function of temperature along the computed LOS. These calculations would systematically skew results toward a few ions that are preferentially formed at the chosen temperatures. Therefore, a modified approach is needed.

Consider the factorization of the population density n_j into two components:

$$n_j = n'_j \cdot \frac{n_{\text{ion}}}{n_{\text{el}}}, \quad (4)$$

where

$$n'_j = \frac{n_j}{n_{\text{ion}}} \frac{n_{\text{el}}}{n_{\text{H}}} \frac{n_{\text{H}}}{n} n, \quad (5)$$

n_{ion} is the population density of the ion to which line i belongs, n_{el} is the number density of all ions of that element, n_{H} is the number density of hydrogen nuclei, and n is the electron density. Then, including the label k again, equation (1) becomes

$$I_k = \frac{hc}{\lambda_k} \frac{1}{4\pi} A_k \int_{-\infty}^0 n'_{j(k)}(s) \frac{n_{\text{ion}}}{n_{\text{el}}} ds. \quad (6)$$

The ionization fraction, $n_{\text{ion}}/n_{\text{el}}$, implicitly including the label k , is a strong function of the electron temperature T_e and a weak function of all other parameters. It depends on bound-free rate coefficients for processes that involve mostly electron collisions and can be written $Y_k(T_e)$. In contrast, for all lines considered here, the term $n'_{j(k)}(s)$ is a relatively weak function of T_e but is also a function of the incident radiation intensity, and thus the radius r , and on n . It depends primarily on bound-bound rate coefficients and thus can be written $X_k(T_e, n, r)$. (The dependence of variables T_e , r , and n on s is implicitly assumed here). Then,

$$I_k = \frac{hc}{\lambda_k} \frac{1}{4\pi} A_k \int_{-\infty}^0 X_k(T_e, n, r) Y_k(T_e) ds. \quad (7)$$

As noted above, the term $Y_k(T_e)$ depends more sensitively on T_e than the term $X_k(T_e)$. Ionization rate coefficients determining $Y_k(T_e)$ scale as $\exp(-I/kT_e)$, where $I/kT_e \gg 1$. Excitation rate coefficients determining $X_k(T_e)$ scale as $\exp(-E/kT_e)$, where $E/kT_e \ll 1$ for transitions between levels with the same principal quantum number. Thus, a distribution of material of various temperatures along the LOS influences the term $Y_k(T_e)$ with little influence on the term

$X_k(T_e, n, r)$. Equation (7) can then be split as follows:

$$I_k = \frac{hc}{\lambda_k} \frac{1}{4\pi} A_k \int_{-\infty}^0 X_k(T_e, n, r) ds \langle Y_k \rangle, \quad (8)$$

where the quantity $\langle Y_k \rangle$ must satisfy

$$\int_{-\infty}^0 X_k(T_e, n, r) Y_k(T_e) ds = \int_{-\infty}^0 X_k(T_e, n, r) ds \langle Y_k \rangle, \quad (9)$$

i.e., $\langle Y_k \rangle$ is defined to be the average value of the ionization fraction to which the line k belongs, weighted by $X_k(T_e, n, r)$, along the LOS. This is manifestly different for all lines. If a suitable approximation for $\langle Y_k \rangle$ can be derived, then the intensity for each line k can be calculated using equation (8) and not equation (7). Such an approximation can be estimated using the differential emission measure (e.g., Craig & Brown 1976). For all lines of interest, the detailed calculations discussed below show that $X_k(T_e, n, r) \propto n^\alpha$, where α is in the range 1 to 2. Then equation (9) can be written

$$\int_{-\infty}^0 n^\alpha Y_k(T_e) ds = \int_{-\infty}^0 n^\alpha ds \langle Y_k \rangle. \quad (10)$$

Transforming from an integration over path length, ds , to one over logarithmic temperature $T = \log_{10} T_e$, one can define the differential emission measure $\xi(T)$ such that

$$n^2 ds = \xi(T) dT; \quad (11)$$

then equations (9) and (11) give

$$\int_{\Delta T} \xi(T) n^{\alpha-2} Y_k(T) dT = \int_{\Delta T} \xi(T) n^{\alpha-2} dT \langle Y_k \rangle. \quad (12)$$

Analysis of EUV emission lines from disk spectra of the quiet Sun show that $\xi(T)$ has a peak near $T = 6.2$, dropping to $1/e$ of the peak intensity at $T = 5.9$ and 6.5 (e.g., Raymond & Doyle 1981; Dere & Mason 1993). A reasonable approximation, given that disk spectra are heavily weighted toward the coronal base anyway and that, therefore, there is little information from such spectra on the form of $\xi(T)$ beyond roughly $1.2 R_\odot$, is to assume that this can be approximated by a constant value, i.e., $\xi(T) \simeq \xi_c$, between $T = 5.9$ and 6.5 , and zero otherwise. While this approximation ignores details of the peak in $\xi(T)$ near $T = 6.2$, it does yield a form for the expression for the line intensity, which separates into the two simple factors in equation (8). Using $\xi(T) = \xi_c$ and $\Delta T = 0.6$ and ignoring any weak dependence of $n^{\alpha-2}$ on T , equation (12) yields

$$\langle Y_k \rangle \simeq \frac{1}{0.6} \int_{5.9}^{6.5} Y_k(T) dT. \quad (13)$$

Physically, $\langle Y_k \rangle$ is the average value of the ionization fraction over the logarithm of the electron temperature range 5.9–6.5. Ionization balance calculations solving for $Y_k(T)$ were made using rate coefficients of Arnaud & Raymond (1992), modified for finite electron densities as discussed by Judge et al. (1995), and values of $\langle Y_k \rangle$ were determined for each ion. They are tabulated in Table 3.

Line intensities were calculated as follows: values of $\langle Y_k \rangle$ were computed from an ionization balance calculation ignoring all levels but those belonging to ground terms. Then, a radial distribution of coronal density with radius was adopted. The following formula was used as a simple analytic fit to the radius r (in solar units, $R_\odot = 7 \times 10^{10}$

TABLE 3
COMPUTED INTENSITIES AT 1.1 R_{\odot}

Sequence	Ion	Transition ($j \rightarrow i$)	λ (μm)	$\langle Y_k \rangle$	A (s^{-1})	$-\log_{10} \frac{n_j A_{ji}}{n_{\text{ion}} n}$ ($\text{cm}^3 \text{ s}^{-1}$)	$-\log_{10} \frac{n_j^0 A_{ji}}{n_{\text{ion}} n}$ ($\text{cm}^3 \text{ s}^{-1}$)	$\log_{10} I$	$-\left(\frac{d \ln I}{dr}\right)^{-1}$ (R_{\odot})
Be	Si XI	$^3P_{2 \rightarrow 1}^o$	1.933	0.071	1.80(0)	9.84	9.80	-1.43	0.067
B	Si X	$^2P_{3/2 \rightarrow 1/2}^o$	1.430	0.142	2.97(0)	8.19	8.41	0.73	0.088
	Mg VIII	$^2P_{3/2 \rightarrow 1/2}^o$	3.03	0.073	3.10(-1)	8.74	8.76	-0.36	0.106
C	Mg VII	$^3P_{1 \rightarrow 0}$	9.03	0.030	2.55(-2)	9.96	9.95	-2.34	0.151
		$^3P_{2 \rightarrow 1}$	5.50		8.24(-2)	9.33	9.33	-1.56	0.118
	Si IX	$^3P_{1 \rightarrow 0}$	3.93	0.169	3.03(-1)	8.81	8.84	-0.17	0.123
		$^3P_{2 \rightarrow 1}$	2.585		7.91(-1)	8.67	8.82	-0.06	0.086
	S XI	$^3P_{1 \rightarrow 0}$	1.920	0.154	2.51(0)	8.10	8.55	-0.04	0.101
		$^3P_{2 \rightarrow 1}$	1.393		5.08(0)	8.56	8.88	-0.44	0.073
	Ar XIII	$^3P_{1 \rightarrow 0}$	1.016	0.121	1.72(1)	7.77	8.67	-0.19	0.095
		$^3P_{2 \rightarrow 1}$	0.8300		2.25(1)	8.83	9.06	-1.26	0.068
	Ca XV	$^3P_{1 \rightarrow 0}$	0.5695	0.033	9.56(1)	7.79	8.52	-0.30	0.090
		$^3P_{2 \rightarrow 1}$	0.5445		8.28(1)	8.89	8.91	-1.46	0.065
N	S X	$^2D_{5/2 \rightarrow 3/2}^o$	8.68	0.225	2.42(-2)	10.81	10.79	-3.31	0.075
O	Si VII	$^3P_{1 \rightarrow 2}$	2.481	0.027	1.52(0)	8.68	8.94	-0.71	0.094
		$^3P_{0 \rightarrow 1}$	6.51		2.02(-1)	9.96	9.96	-2.42	0.090
	S IX	$^3P_{1 \rightarrow 2}$	1.252	0.178	1.14(1)	8.36	8.98	-0.07	0.091
		$^3P_{0 \rightarrow 1}$	3.76		9.81(-1)	9.77	9.75	-2.02	0.073
	Ar XI	$^3P_{1 \rightarrow 2}$	0.6918	0.184	6.74(1)	8.32	9.13	-0.41	0.091
		$^3P_{0 \rightarrow 1}$	2.619		2.84(0)	9.88	9.84	-2.62	0.068
	Ca XIII	$^3P_{0 \rightarrow 1}$	2.258	0.155	4.16(0)	10.04	9.99	-2.55	0.067
F	S VIII	$^2P_{1/2 \rightarrow 3/2}^o$	0.9916	0.087	1.86(0)	9.00	9.11	-0.97	0.076
	Ar X	$^2P_{1/2 \rightarrow 3/2}^o$	0.5522	0.208	1.06(2)	8.60	9.46	-0.54	0.091
Mg	Fe XV	$^3P_{2 \rightarrow 0}^o$	0.5023	0.098	7.80(-3)	13.10	13.09	-3.85	0.065
		$^3P_{2 \rightarrow 1}$	0.7062		3.37(1)	9.46	9.46	-0.37	0.065
Al	Ca VIII	$^2P_{3/2 \rightarrow 1/2}^o$	2.321	0.006	7.19(-1)	8.58	8.77	-2.42	0.096
	Fe XIV	$^2P_{3/2 \rightarrow 1/2}^o$	0.5304	0.087	6.02(1)	7.84	7.97	1.36	0.073
Si	Fe XIII	$^3P_{1 \rightarrow 0}$	1.075	0.111	1.40(1)	7.71	8.11	1.35	0.091
		$^3P_{2 \rightarrow 0}$	0.5386		6.35(-3)	11.45	11.50	-2.17	0.068
		$^3P_{2 \rightarrow 1}$	1.080		9.87(0)	8.25	8.31	0.72	0.068
S	Ni XIII	$^3P_{1 \rightarrow 2}$	0.5117	0.073	1.57(2)	8.56	9.78	-0.77	0.095
		$^3P_{0 \rightarrow 1}$	19.30		6.84(-3)	11.43	11.42	-5.18	0.109
	Fe XI	$^3P_{1 \rightarrow 2}$	0.7894	0.100	4.38(1)	8.16	8.49	0.96	0.084
		$^3P_{0 \rightarrow 1}$	6.08		2.26(-1)	9.98	9.95	-1.68	0.103
		$^3F_4^o \rightarrow ^3D_3^o$	0.6936		5.81(0)	11.12	11.12	-2.00	0.065
		$^3G_4^o \rightarrow ^3F_4^o$	0.5203		6.31(0)	11.02	11.03	-1.79	0.064
Cl	Fe X	$^2P_{1/2 \rightarrow 3/2}^o$	0.6376	0.108	6.94(1)	8.10	8.26	1.12	0.074
		$^4F_{7/2 \rightarrow 9/2}$	1.945		4.26(0)	10.26	10.28	-1.56	0.065
		$^2F_{7/2} \rightarrow ^4F_{7/2}$	0.5542		6.12(0)	10.48	10.48	-1.24	0.065
		$^2F_{7/2} \rightarrow ^4F_{5/2}$	0.7076		5.43(0)	10.53	10.53	-1.40	0.065
		$^2G_{9/2} \rightarrow ^2F_{7/2}$	1.009		4.69(0)	11.01	11.01	-2.03	0.065
		$^2G_{7/2} \rightarrow ^2F_{7/2}$	0.9762		6.10(0)	10.74	10.74	-1.74	0.065
Ar	Fe IX	$^3P_{2 \rightarrow 1}^o$	1.868	0.110	2.07(0)	10.77	10.76	-2.03	0.066
		$^3F_3^o \rightarrow ^3P_2^o$	0.6393		5.06(-2)	10.52	10.70	-1.23	0.091
		$^3F_{3 \rightarrow 4}^o$	2.856		1.07(0)	9.19	9.37	-0.56	0.091
		$^3F_{2 \rightarrow 3}^o$	2.218		3.11(0)	9.55	9.78	-0.88	0.070
		$^1F_3^o \rightarrow ^3D_3^o$	0.9788		7.77(0)	10.73	10.73	-1.72	0.065
		$^1F_3^o \rightarrow ^1D_2^o$	1.102		2.01(0)	11.32	11.32	-2.36	0.065

NOTE.—Intensities are in units of $\text{ergs cm}^{-2} \text{ s}^{-1} \text{ st}^{-1}$. Einstein A -coefficients use the notation $x \cdot y(z) \equiv x \cdot y \times 10^z$. Wavelengths, from the CHIANTI database, are generally accurate to one part in 10^3 (see the Appendix).

cm), from density data tabulated by Allen (1973) § 84:

$$n(r) = n_0 \left[a \cdot \exp\left(-\frac{r-1}{h}\right) + \left(1 - a - \frac{1}{b}\right) \cdot \exp\left(-\frac{r-1}{d \cdot h}\right) + \frac{1}{br^3} \right]. \quad (14)$$

Parameters applicable to the solar minimum equatorial coronal density data were adopted: $n_0 = 2 \times 10^8 \text{ cm}^{-3}$, $a = 0.8$, $b = 30$, $d = 3$. This yields densities that match Allen's tabulated values to within 0.1 dex and that lie between the tabulated solar minimum polar and solar maximum densities of Allen (1973). In this loose sense, the densities used represent an average coronal density struc-

ture. The scale height h corresponds to an atmosphere in hydrostatic equilibrium at 10^6 K. The cubic term represents a solar wind component accelerating as $v(r) \propto r$. Using these densities, fixed abundances were adopted (Table 1), an electron temperature of 10^6 K was used, and level populations for levels within each ion were computed to determine $X_k(T_e, n, r)$ as a function of radius, out to $20 R_\odot$. LOS integrations were performed numerically to determine $\int_{-\infty}^0 X_k(T_e, n, r) ds$ in equation (8), and the intensities were evaluated by this equation.

Note that the approximation embodied in equation (8) is intended to be used for calculation of average intensities as a function of projected height above the solar limb. Several data sets show that this approximation must be invalid for studying particular coronal structures (see Penn et al. 1994 and references therein).

3.3.3. Calculations of Level Populations within Each Ion

Number densities n'_j [equivalently $X_k(T_e, n, r)$] were obtained for a given atomic model, which includes levels from just an individual ion (details below), for specific electron densities, temperatures, and radiation fields. The incident photospheric radiation was computed using a Planck function at 5900 K, multiplied by the usual dilution factor

$$W = \frac{1}{2} \left[1 - \sqrt{1 - \left(\frac{R_\odot}{r} \right)^2} \right], \quad (15)$$

where R_\odot is the solar radius. Care was taken to include excited energy levels in each ion that can influence the IR forbidden lines through electron collisional excitation followed by radiative decay. Thus, all levels with the same principal quantum number as the ground level were included for all ions, and all higher levels were ignored. Calculations were made using the latest available rate coefficients. Extensive use was made of the CHIANTI compilation (Dere et al. 1997), which includes electron collisional processes largely from the volume edited by Lang (1994) and radiative transition probabilities from a variety of sources. Forbidden radiative transition probabilities were taken from Kaufman & Sugar (1986), with the exception of ions of the Be sequence, which were taken from Brage et al. (1997). While proton collisions are known to be significant for some ions (e.g., Flower & Pineau des Forêts 1973; Sahal-Bréchet 1974), their influence for electron temperatures of 10^6 K and above is relatively small for IR transitions compared with electron collisions and radiative excitation, and they have been neglected in these calculations.

3.3.4. Uncertainties

Uncertainties in these calculations are difficult to assess accurately because errors arise both in the atomic parameters affecting level populations and in our understanding of the coronal plasma properties, especially the distribution of emitting material with temperature. Aside from negligible errors in atomic constants (including transition wavelengths), the smallest errors almost certainly arise from the term $X_k(T_e, n, r)$. With some potential exceptions discussed below, the maximum likely error in these terms is a factor of 2, and more likely closer to 10%–20%, on the basis of error estimates in collisional excitation rate coefficients (e.g., see the discussions in the volume edited by Lang 1994) and in forbidden line radiative transition probabilities (Kaufman & Sugar 1986).

The largest sources of error arise in the use and calculation of the term $\langle Y_k \rangle$. First, the separation of the integral equation (7) into the form of equation (8) of course makes the assumption that this is meaningful for all lines. Furthermore, there is the crucial assumption that the differential emission measure is constant between logarithmic temperatures of 5.9 and 6.5, and zero outside this range, and that this is valid *at all radial distances in the corona*. Thus, even if the ionization balance as a function of temperature is free of error (this is not true), these assumptions are unlikely to be correct at least at all heights in the corona, and potentially large, systematic errors may arise. At this stage, it seems best to simply recognize this source of uncertainty and try not to overinterpret comparisons between certain ions and their behavior as a function of radius.

3.3.5. Results

The transitions in Table 2 belong to sequences isoelectronic with the elements Be, B, C, N, O, F, Mg, Al, Si, P, S, Cl, and Ar. The first detailed calculations were therefore done for the ions of each isoelectronic sequence that are, on the basis of Table 2, expected to be brightest. In order of isoelectronic sequence (equivalently number of electrons around the nuclei), these are Si xi, Si x, Si ix, S x, S ix, Ar x, and Fe xv through Fe ix. The resulting line intensities and their gradients with projected height above the limb at $r = 1.1 R_\odot$ are listed in Table 3, together with additional ions discussed below. The table lists components of equation (8) and includes intensities computed both with and without the influence of photospheric radiation in the calculations of $X_k(T_e, n, r)$.

Figure 1 shows the dependence of the intensities I_k of the 10 strongest lines (ordered using units of photons $\text{cm}^{-2} \text{s}^{-1} \text{st}^{-1}$, since modern IR detectors count photons) as a function of projected radial height above the solar limb (*upper panel*). In the lower panel, the ratio of the intensities computed with photospheric radiation to those computed without are shown. Inspection of the results in the table, for the ions representing the strongest transitions of specific isoelectronic sequences, reveals the following results:

1. As anticipated in the Appendix, forbidden lines arising from transitions between excited levels are substantially weaker than those arising from transitions between the ground levels (compare the IR line of Si xi, a transition between excited levels in the Be isoelectronic sequence, with other ions of silicon in the table, for example). In particular, all forbidden lines from ions of the Be, N, and P sequences are more than a factor of 10 weaker than the strongest lines, and those of the Mg and Ar sequences are a factor of 10 or so weaker. These and other ions of these isoelectronic sequences can therefore be discounted as candidates for Zeeman measurements.

2. The excitation of essentially all remaining forbidden lines, i.e., of the B, C, O, Al, Si, S, and Cl sequences, have strong contributions from photoexcitation by the photospheric radiation. This is indicated by a comparison between the calculations with and without this process (Fig. 1, lower panel).

3. The largest influence of photoexcitation occurs in excitation of the lowest transition² ($J = 1 \rightarrow 0$) in ions of the C and Si sequences and the lowest transition ($J = 1 \rightarrow 2$) in

² Here and henceforth, the notation used is that of higher level \rightarrow lower level.

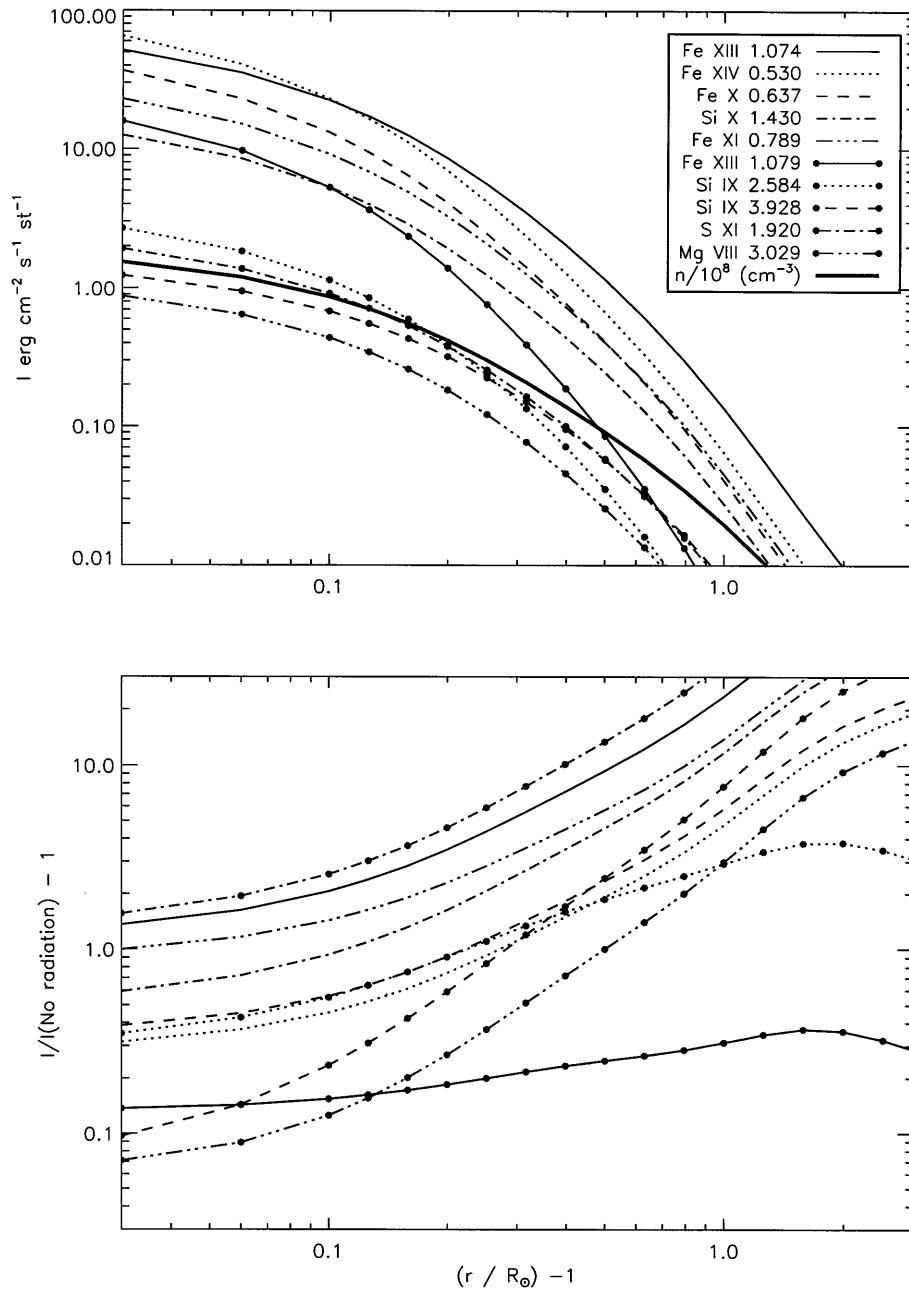


FIG. 1.—Dependence of the computed line intensities for the 10 strongest lines (evaluated at $r = 1.1 R_{\odot}$; in units of photons $s^{-1} \text{st}^{-1}$) in the visual and IR regions of the solar coronal spectrum. *Lower panel:* ratio of the intensities computed with and without the inclusion of photospheric radiation in the excitation calculations (i.e., the P_{ij} and P_{ji} terms in eq. [2]). The radial behavior of the electron density n is also shown (*thick line*) in the upper panel. Note that the intensities of some lines that are strongly affected by photoexcitation, for instance that of Fe XIII at $1.0747 \mu\text{m}$, follow a radial dependence similar to n to the first power, while others (e.g., Fe XIII $1.0798 \mu\text{m}$) behave more like n to the second power.

the O and S sequences. These transitions might therefore be expected to give a strong fluorescent polarization signal that is comparable to or stronger than the several tens of percent computed for the equivalent ($J = 1 \rightarrow 0$) transition in Fe XIII (Si-like) by Sahal-Br  chot (1977). Additional calculations would be needed to assess the expected degree of linear polarization for each ion.

4. The magnitudes of the computed forbidden line intensities of these particular lines are in satisfactory agreement with those measured by, e.g., Jefferies, Orrall, & Zirker (1971) at optical wavelengths and by Kuhn, Penn, & Mann (1996) at IR wavelengths. More careful comparisons with observations are made below.

3.3.6. Additional Calculations and Spectral Synthesis

Encouraged by the initial success of these first results, detailed calculations were performed for the other abundant ions of Table 2. Based upon the detailed results above, only those ions belonging to the B, C, O, Al, Si, S, and Cl sequences that appear in Table 2 are likely to be strong enough to warrant further study. The results of these additional calculations are also listed in Table 3 and are presented graphically in the synthetic spectra shown in Figure 2. The figure includes contributions to the intensities from the K corona at a level of $1/10^6$ of the solar photospheric intensity, which is a reasonable estimate of typical conditions at some of the best high-altitude coronagraphic sites, for a

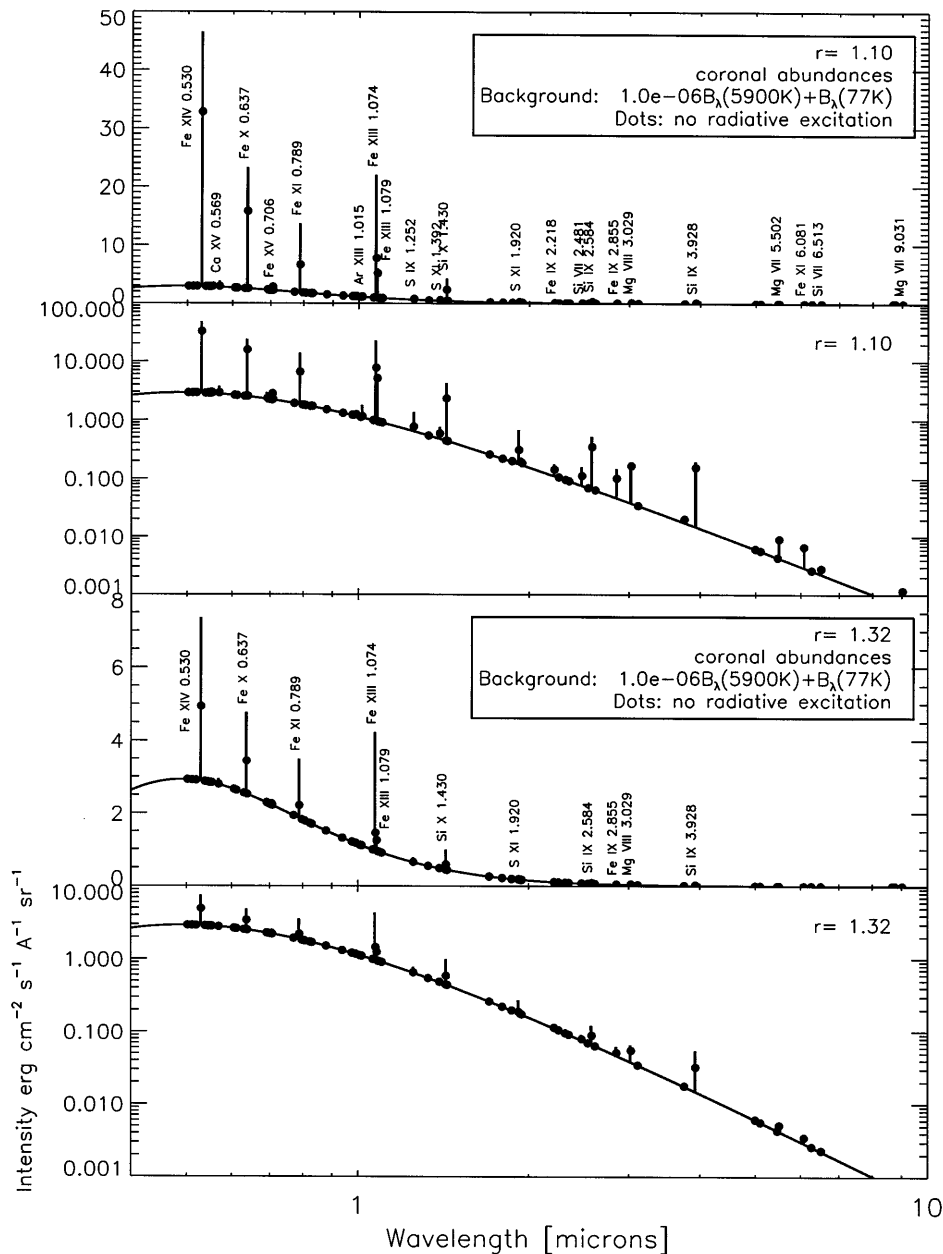


FIG. 2.—Synthetic emission line spectra evaluated at 1.1 and 1.3 R_{\odot} and including typical intensities of the K corona (the F corona is negligible at these heights) from Münch (1966) and thermal emission from an instrument cooled to liquid nitrogen temperatures (a 77 K blackbody spectrum). The unit of intensity is $\text{ergs cm}^{-2} \text{s}^{-1} \text{\AA}^{-1} \text{sr}^{-1}$, and line intensities plotted are peak intensities assuming a line width (FWHM) of 30 km s^{-1} in Doppler units (thus, peak intensities are approximately integrated intensities I_k divided by wavelength λ_k measured in microns). No other source of IR light is included in this plot (e.g., from thermal emission/scattering from the Earth's atmosphere). Line identifications are marked (arbitrarily) for lines whose peak intensities exceed 20% of the neighboring background intensity.

wavelength near $1 \mu\text{m}$ (e.g., Golub & Pasachoff 1997, pp. 143 and 147).

The list of ions in Table 3 should contain all of the strong coronal emission lines between 1 and $10 \mu\text{m}$. Figure 2 should similarly contain all of the strongest coronal emission lines. Atomic data were from the sources discussed above, except that electron excitation collisional data for Ca VIII were taken from the homologous ion Mg VIII, since no data for this ion could be found. For Ni XIII, collisional data

for Fe XI were adopted in the absence of any specific data.³

Aside from illustrating the strongest coronal transitions

³ This could be substantially in error. Ions of the S sequence require special attention since the $J = 1$ and 0 levels cross over between Ni XIII and Cu XIV, owing to the transition from LS to jj coupling. Furthermore, the Ni XIII 0.512 \AA line is computed to be an order of magnitude weaker than observed (see § 4). The data used here are based upon perturbation theory in the Schrödinger formulation of quantum mechanics. More detailed relativistic atomic structure calculations appear to be warranted for these ions (T. Brage 1995, private communication).

TABLE 4
CANDIDATE LINES FOR THE APPLICATION OF
STOKES POLARIMETRY TO DETERMINE
CORONAL MAGNETIC FIELDS

Ion	Wavelength (μm)
Fe XIV	0.530
Fe X	0.637
Fe XI	0.789
Fe XIII	1.0747
Fe XIII	1.0798
Si X	1.430
S XI	1.920
Si IX	2.584
Fe IX	2.855
Mg VIII	3.028
Si IX	3.929
Mg VII	5.502
Mg VII	9.031
Fe XI	6.081 ^a
Ni XIII	19.3 ^a

^a These lines are computed to be very weak; they are included because of their favorably long wavelengths and potential problems with the atomic data used (see text).

present in the IR spectrum, Figure 2 illustrates a fundamental trend. The strongest lines (measured either in photon or energy units) lie in the optical and near-IR regions below $\sim 1 \mu\text{m}$. Lines become substantially weaker at longer wavelengths (with the previously noted caveat that the interesting S sequence ions of Fe XI and Ni XIII require further work). Those beyond $10 \mu\text{m}$ (see Table 2 for many examples) are probably too weak for the high signal-to-noise ratio requirements for magnetograph measurements.

The physical reasons for this are simple. Almost all of the transitions discussed here are magnetic dipole (M1) transitions. Atomic line strengths being equal (they do not depend strongly on ion charge for M1 transitions), the Einstein A -coefficients scale with transition wavelength λ_k as λ_k^{-3} . Transitions induced by electron collisions tend to have higher probabilities for M1 transitions which lie further in the IR region, simply because for a given isoelectronic sequence, the collisional probabilities are largest for ions of lowest charge, i.e., those having the longest wavelengths in M1 transitions. Photon escape in other (electric dipole) transitions sharing a common upper level, when present, is more likely for longer wavelength transitions for similar reasons. Thus, the probabilities of photon escape in a given M1 line tend to decrease rapidly with increasing λ_k . Furthermore, radiative excitation probabilities decrease with increasing wavelength λ_k . Einstein B -coefficients are independent of λ_k for a fixed atomic line strength, but the intensity of the incident photospheric radiation varies according to λ_k^{-1} in the Rayleigh-Jeans limit. All of these processes serve to produce the sharp decrease in the intensity of IR coronal lines with wavelength seen in Figure 2.

Finally, on the basis of Figure 2, Table 4 lists the most likely candidates for application to Stokes measurements of the Zeeman effect, assuming that the calculations are consistent with available observations. Note that the wavelengths are generally not reliable to better than three significant figures (see the Appendix).

4. INITIAL COMPARISON WITH OBSERVATIONS

Detailed comparisons of observed and computed intensities are not yet warranted given that the adopted density structure is just a spatial “average” that probably cannot exist at any given time on the Sun. Furthermore, no complete spectrum exists that simultaneously covers the optical and IR region. Nevertheless, comparisons of computed intensities with those that are available can be made to see if the calculations are in rough agreement in terms of average intensities and to see if their measured dependence with projected height above the solar limb is reasonable.

There are several sources of optical and IR data. Between 0.3 and $0.8 \mu\text{m}$, Jefferies et al. (1971) list line intensities measured at two heights in “coronal condensations” seen at the 1965 May 30 total eclipse. Kuhn et al. (1996) list intensities (and useful upper limits) of lines between 1 and $1.5 \mu\text{m}$ from the total eclipse of 1994 November 3 that may be considered to be from a similar type of coronal condensation as that measured by Jefferies et al. (1971). The observations of Kuhn et al. (1996) are probably of the highest quality and should be given extra weight. Finally, beyond $1.5 \mu\text{m}$, the only published work to claim detections are the 1 – $3 \mu\text{m}$ grating data of Münch et al. (1966), from the 1996 November 12 total eclipse, and FTS data from Olsen et al. (1971), from the 1970 March 7 total eclipse. Note that the intensities of the latter are questioned by Penn & Kuhn (1994), who suggested that these early measurements overestimated line intensities.

Figure 3 shows a comparison between observed and computed data, taking all data at face value. For each set of observations, the computed intensities were evaluated through lines of sight passing through the radii in the POS marked in the figure (so a value of $1.03 R_\odot$ was used for the data of Münch, Neugebauer, & McCammon 1966, for example). Considering the levels of approximation in the calculations (see § 3.3.4) and the diverse set of observations, the observed and computed data can be regarded as being consistent with one another (note that the figure is plotted in the log-log plane). A scatter of a factor of 2 is seen around equality, with the exception of [Ni XIII] at $0.512 \mu\text{m}$, which is an order of magnitude too weak in the calculations compared with iron lines (data are from Jefferies et al. 1971). This may result from inadequate treatment of collision strengths and transition probabilities for ions in the S sequence (discussed above). [S XI] $1.392 \mu\text{m}$ is computed to be an order of magnitude stronger than might be inferred from a glance at Table 1 of Kuhn et al. (1996). It is not shown in the figure since the data tabulated by Kuhn et al. (1996) are upper limits to intensities without correction for atmospheric absorption, and at this wavelength it is nearly 100% (J. Kuhn 1997, private communication).

One more important comparison of the calculations with observations can be made. Kuhn et al. (1996) show, in their Figure 3a, the dependence of the intensity of the [Fe XIII] $1.0747 \mu\text{m}$ line with projected height above the lunar limb. This can be directly compared with the calculations shown in Figure 1. Close to the solar limb, the $1/e$ scale height of the observed intensity with projected height is $\sim 0.18 R_\odot$. In the calculations, this is $\sim 0.09 R_\odot$. The intensity of [Fe XIII] lines is computed to vary roughly with electron density n^α , where α is 1 or a little higher (see Fig. 1). This discrepancy suggests several possibilities. It is likely that the density structure at the time of the observations differs sig-

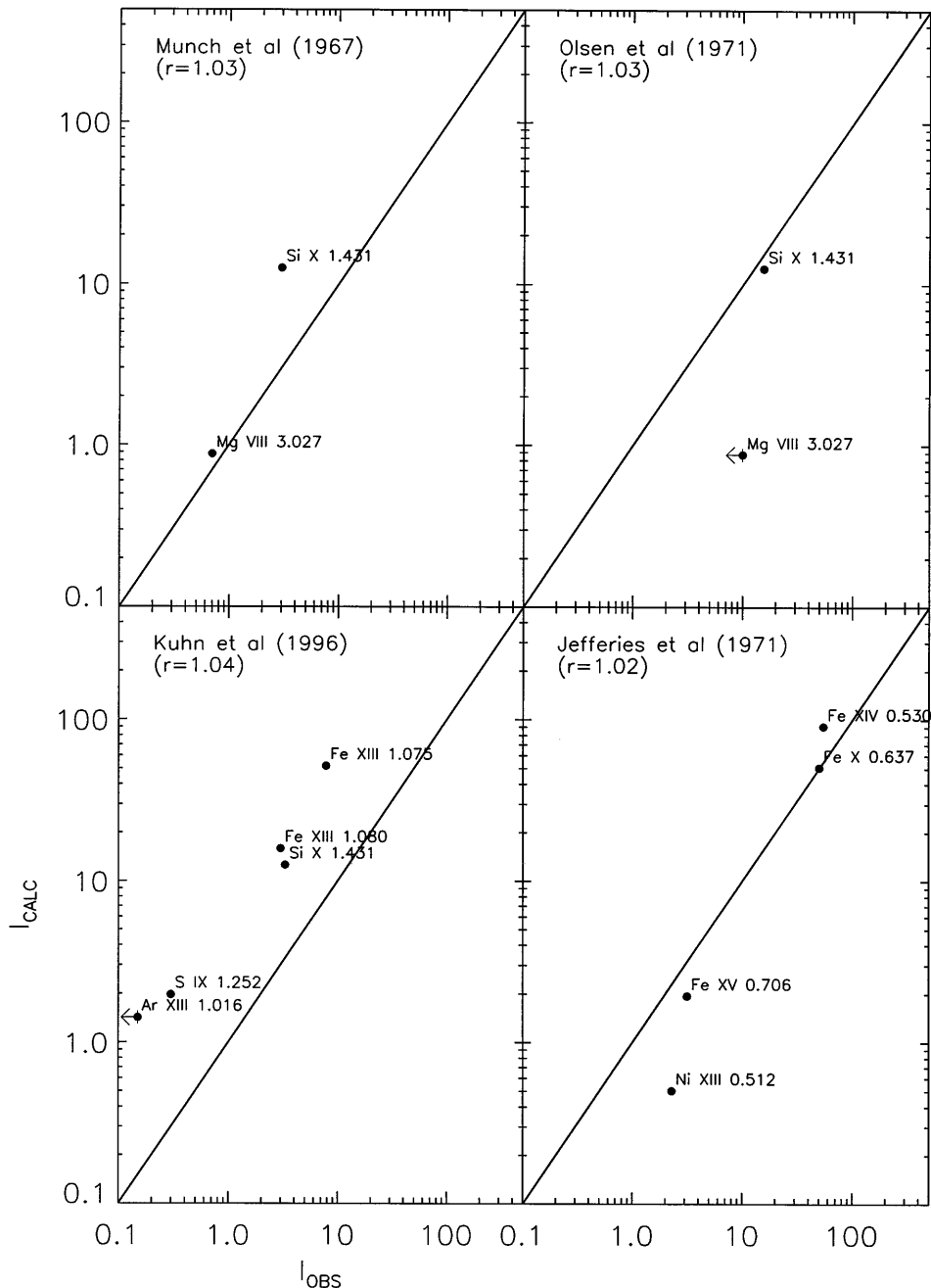


FIG. 3.—Scatter plots showing observed and computed frequency-integrated intensities of IR lines. Data are from a heterogeneous set of observations, and computations are from an “average” coronal density distribution, so comparisons can be made only roughly. Error bars are difficult to assess in both observed and computed data (see text).

nificantly from the “average” structure represented by equation (14). There may be a problem with the interpretation that the radial falloff of the Fe XIII line intensity observed by Kuhn et al. (1996) has a completely solar origin. The latter probably cannot be completely discounted, given the concerns expressed by Kuhn et al. (1996) about the presence of cirrus clouds during the observations. Another more serious possibility is that something crucial is missing from the calculations. The most likely candidate is the assumed dependence of the differential emission measure on projected height (see § 3.3.4).

In conclusion, the agreement between observed and computed intensities at a specific height in the corona is satisfactory. Where comparisons are possible, relative intensities between different lines are in quite good agreement with just

one noted exception. It is reasonable to assume that the theoretical calculations can be used for their primary task specified in § 1: to identify those strong lines that should be considered as candidates for Zeeman determinations of the coronal magnetic field.

The lack of agreement of computed and observed radial dependence for the Fe XIII 1.0747 μm line is more worrisome, but the current uncertainties in treatment of emission measures and in the interpretation of data acquired under variable atmospheric absorption conditions preclude a definitive conclusion.

5. SUMMARY AND CONCLUSIONS

New calculations of the intensities of the forbidden line

spectrum of the corona have been presented using the best currently available atomic data. Several transitions of the B, C, O, Si, and S isoelectronic sequences are sufficiently strong, at least at wavelengths up to $4 \mu\text{m}$, that they are potentially of great interest as diagnostics of the coronal magnetic field through the Zeeman effect. Most of these lines also have the desirable property of falling relatively slowly with projected height above the solar limb (see Fig. 1). They are listed in Table 4. Computed intensities are in reasonable agreement with the observed coronal spectrum, where such data are available. Ions of the S sequence, especially Fe XI and Ni XIII, deserve new atomic structure calculations in the relativistic formalism.

Half of the most promising lines listed in Table 4 have not been observed before and warrant observational study. Most of these lie in atmospheric transmission windows and could in principle be observed from the ground. Portions of the coronal spectrum between 1 and $10 \mu\text{m}$ will be acquired by a joint NSO/NCAR/Rhodes College/Lindau experiment during the 1998 February 26 total eclipse to search for some

of the strongest predicted lines. An important aim will be to determine the radial dependence of the IR emission of at least one IR line, simultaneously with a determination of the radial dependence of the electron density from the polarized brightness of white light. Such measurements are needed to assess the completeness and accuracy of the theoretical intensities computed here. Similar work is worthwhile using existing eclipse data.

Future work should also include attempts to determine the emission measure distribution as a function of projected height above the limb for a variety of structures. Existing data from the CDS and SUMER instruments on *SOHO* would certainly allow such determinations, at least for low projected heights above the solar limb.

The author acknowledges the assistance of R. Meisner for assistance with developing atomic models and thanks Jeff Kuhn and Matt Penn for useful discussions. B. C. Low and Roberto Casini provided useful comments on the manuscript.

APPENDIX A

FINDING STRONG FORBIDDEN LINES IN THE INFRARED SPECTRUM OF THE CORONA

In this Appendix, a first cut through the search for suitable lines is described. Elimination of candidate lines was done on the basis of ion charge, abundance, types of transitions, and considerations of atomic processes that determine the strength of the transitions. More than 50 potentially interesting lines with $\lambda > 1 \mu\text{m}$ survive (Table 2) and are discussed in more detail in the main text.

A1. ABUNDANCE CONSIDERATIONS

Given the measurements of the [Fe XIII] line reported by Kuhn (1995) and that this is one of the strongest forbidden lines in the coronal spectrum, the search can be limited to lines of elements whose "coronal" abundances (e.g., Grevesse & Anders 1991) are at least 1/100 of that of iron, i.e., H, He, C, N, O, Ne, Na, Mg, Al, Si, S, Ar, Ca, Cr, Fe, and Ni. The first five elements are not useful because they contain no suitably strong IR emission lines (see below). Adopted abundances for the remaining elements are listed in Table 1.

A2. ELIMINATION OF TYPES OF TRANSITIONS

IR transitions in highly ionized ions occur between levels of the same terms (forbidden transitions) or between highly excited Rydberg states (allowed transitions). The latter will have extremely weak intensities, since the levels will essentially be populated only by dielectronic recombination, which has rate coefficients several orders of magnitude smaller than the rate coefficients for collisional excitation. Thus, only the forbidden transitions in ground terms and metastable terms need further consideration, since other levels will have negligible populations due to the rapid decay to the ground levels in permitted transitions. This is corroborated by the exploratory work of Chang & Deming (1995).

There are thus just two types of forbidden transitions of interest here. The first are transitions between levels in the ground term of the ions. These belong to the B, C, O, and F and the homologous Al, Si, S, and Cl sequences and include the well-studied [Fe XIV] $0.5304 \mu\text{m}$ green line (Al sequence) and the [Fe XIII] $1.0747 \mu\text{m}$ line (Si sequence). The second are transitions between levels of excited metastable terms and include transitions of the He, Be, Ne, Ar, and Mg sequences (triplet metastable terms with opposite parity to the singlet ground term), and N and P sequences (doublet metastable terms of the same parity as the quartet ground term). Transitions of the first kind were treated fully (for wavelengths longer than $1 \mu\text{m}$) by Greenhouse et al. (1993), but the second were treated less completely.

Forbidden transitions of the second kind belonging to ions of the He, F, and Ne isoelectronic sequences are expected to be much weaker than transitions belonging to the first kind. This is because the metastable levels belong to an electron configuration with principal quantum number one greater than that of the ground configuration. Such levels lie at energies greatly in excess of the mean thermal energy under coronal ionization equilibrium conditions.⁴ (The same is not true for ions

⁴ In coronal ionization equilibrium, the thermal energy where an ion reaches maximum abundance scales approximately as $kT_e \propto I_z$, where I_z is the ionization potential of an ion of charge $z - 1$ ($z = 1$ for neutrals, $z = 2$ for singly ionized ions, etc.), and $I_z \propto z^2$ and is in a regime where $I_z/kT_e \geq 20$. Energies E_n of metastable terms with the same principal quantum number n as the ground term, but different angular momentum and spin quantum numbers, scale as the residual electrostatic term in the Hamiltonian, which scales as z^1 , and are thus formed in a regime where $E_n/kT_e \sim 10/z$. Energies E_{n+1} of metastable terms with principal quantum number $n + 1$ scale as z^2 and are thus formed in a regime where $E_{n+1}/kT_e \sim 10$.

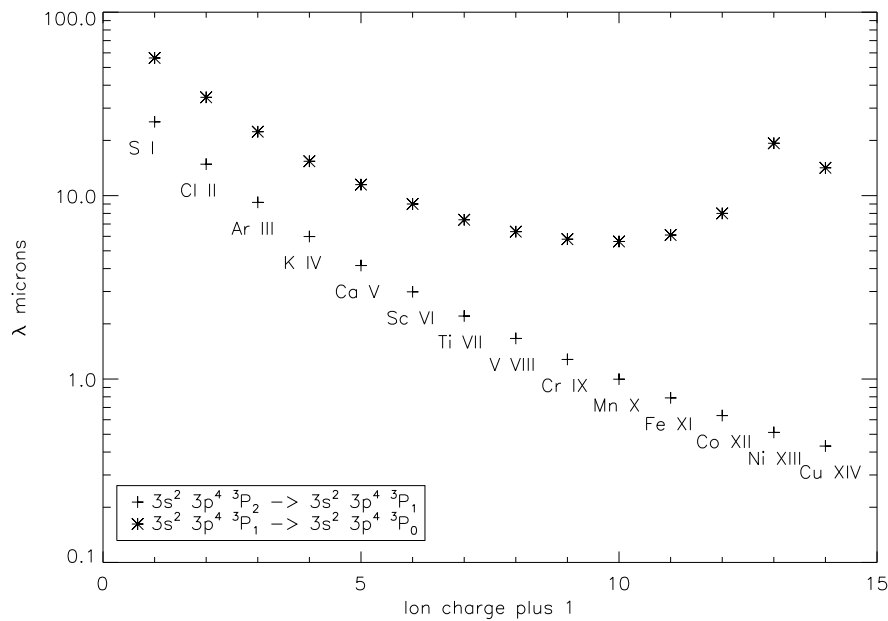


FIG. 4.—Dependence of the energy level splittings of fine structure levels, plotted as the transition wavelength in μm , as a function of ion charge z along the sulfur isoelectronic sequence. (The energy differences in ergs are simply $10^4 hc/\lambda$). The behavior of the plus symbols shows “normal” isoelectronic behavior. The behavior of the asterisks does not. In this case, the $J = 0$ and 1 levels actually cross between Ni XIII and Cu XIV, yielding anomalously long wavelengths for transitions between the $J = 0$ and 1 levels for many ions in this sequence.

of the homologous Cl and Ar sequences, which have metastable quartet levels that have the same principal quantum number as the ground levels).

Transitions of the first kind will in general be stronger than transitions of the second kind for other reasons. The strength of forbidden transitions of the second kind depends primarily on whether the metastable levels have the same parity as the ground term. If not, the upper metastable levels can also decay via intercombination (IC) electric dipole (E1) transitions. For such cases, such as the $nsnp^2\ ^4P_J$, $J = 1/2, 3/2, 5/2$ metastable levels in the B and Al sequences (the levels all have IC transitions to levels of the opposite parity ground term, $ns^2np^2\ ^3P_{1/2,3/2}^o$), the M2 forbidden lines (e.g., $nsnp^2\ ^4P_{5/2} \rightarrow nsnp^2\ ^4P_{3/2}$) are completely negligible. For example, data in the National Institute of Standards and Technology (NIST) database for the Al-like ions Fe XIV and Ni XVI show that the M1 transition probabilities between levels of the $3s3p^2\ ^4P$ term are 6 or more orders of magnitude smaller than the competing electric dipole (E1) intercombination transition probabilities. Given the stronger dependence of the M1 transition probabilities on ion charge z than the intercombination E1 transition probabilities (e.g., the Be- and Mg-like ions are discussed by Brage et al. 1998), these transitions can be safely ignored for all ions of less or equal charge considered here. This lends support to the omission of such terms in the study of Greenhouse et al. (1993).

Metastable levels that have the same parity as the ground levels, or which have opposite parity but cannot decay via IC transitions owing to the J selection rules, decay via M1 and higher order multipole transitions. The IR transitions between levels of such terms are thus likely to have much higher branching ratios. An example is in the Be isoelectronic sequence where the radiative decay routes include just the magnetic quadrupole (M2) transition $2s2p^3\ ^3P_2^o \rightarrow 2s^2\ ^1S_0$ of the $2s2p^3\ ^3P_2$ level is mostly via the forbidden IR transition to the $2s2p^3\ ^3P_1$ level for nuclear charge greater than 8.⁵ Table 3 of Greenhouse et al. (1993) lists branching ratios for this and similar transitions, but they omitted the Ar isoelectronic sequence.

One last aspect of the calculations of Greenhouse et al. (1993) is very useful for reducing the list of lines further, at least for transitions of the first kind. In their Figure 3 they present “critical electron densities,” n_{crit} , i.e., those electron densities at which collisional deexcitation rates of the upper level of a line equal radiative decay rates (their eq. [1]). The line emission coefficient scales with the electron density of the emitting plasma according to $n_{\text{crit}}/(n_{\text{crit}} + n_e) \cdot n_e^2$. The solar corona typically has electron densities $n_e = n_{\text{cor}} \sim 10^8\ \text{cm}^{-3}$. Thus line intensities with $n_{\text{crit}} \ll n_{\text{cor}}$ scale as $n_{\text{crit}}n_{\text{cor}}$, which is $\ll n_{\text{cor}}^2$.

A3. LIST OF PROMISING LINES

Based upon the above criteria, the list of potentially interesting lines is given in Table 2. In summary, it basically consists of lines of ions of all abundant elements (Ne, Na, Mg, Al, Si, S, Ar, Ca, Cr, Fe, and Ni) that have charges between 4 and 14, that belong to transitions between ground or metastable levels of the Be, B, C, N, O, F, Mg, Al, Si, P, S, Cl, and Ar isoelectronic sequences, and that also have large branching ratios and small collisional destruction probabilities.

To derive this a compilation of the energies of atomic levels for all abundant elements was done using the NIST on-line database.⁶ Plots of energy separation between the relevant levels as a function of nuclear charge Z along each isoelectronic

⁵ The Einstein A -coefficients of the forbidden transitions scale with Z to a higher power than the spin-changing transitions owing to the dependence of the transition matrix elements and wavelengths on Z (e.g., Cowan 1981).

⁶ The NIST on-line database, which contains nonrefereed material and is not maintained by the Astrophysical Journal, can be found at http://aeldata.phy.nist.gov/nist_atomic_spectra.html.

sequence were made, and we checked for obvious departures from smooth behaviors (none were found). Some missing data were interpolated using such plots. One interesting isoelectronic plot, for the S sequence, is shown in Figure 4.

The “normal” behavior, qualitatively exhibited by the $J = 2 \rightarrow 1$ transition in Figure 4, shows that the wavelength of a forbidden line decreases smoothly and monotonically with nuclear charge A along an isoelectronic sequence. This follows from the fact that the relativistic terms in the atomic Hamiltonian gradually increase along a sequence. In the isosequences studied here, systematic departures were found for the N and the S sequences, which have wavelengths that are not monotonic with A . For the S sequence, this occurs because the energy levels in fact cross over (i.e., switch order), and near the crossing point, the energy splittings are smaller than they should be. This explains why the $3p^4\ ^3P_0 \rightarrow 3p^4\ ^3P_1$ transitions in Fe XI and Ni XIII have wavelengths closer to 10 and 20 μm than to 1 or 2 μm , as might have been expected from simple extrapolation. These abundant ions therefore fortuitously have much longer wavelengths than they should, owing to a quirk in the atomic physics of their isoelectronic sequence. These will therefore potentially be of interest for Zeeman measurements if they prove to be sufficiently intense.⁷ Calculations for these ions were therefore treated with special care (see the main text).

It should be noted that the wavelengths tabulated, which were taken from the NIST database, are typically accurate only to one part in 10^3 for lines between 1 and 20 μm (see e.g., Greenhouse et al. 1993). Much more accurate data are becoming available through new measurements of low-density astrophysical objects (e.g., Oliva et al. 1994; Feuchtgruber et al. 1997), yielding accuracies of one part in 10^4 or better.

⁷ Note that Ferland (1993) found this same physical effect to be responsible for causing population inversions in the $J = 0 \rightarrow 1$ transitions in the Fe XI ion in calculations of photoionized plasmas.

REFERENCES

- Alissandrakis, C. E., & Kundu, M. R. 1982, *ApJ*, 253, L49
 Allen, C. W. 1973, *Astrophysical Quantities* (London: Athlone Press)
 Arnaud, J., & Newkirk, G., Jr. 1987, *A&A*, 178, 263
 Arnaud, M., & Raymond, J. 1992, *ApJ*, 398, 394
 Brage, T., Judge, P. G., Aboussaid, A., Godefroid, M. R., Jönsson, P., Yunnerman, A., Fischer, C. F., & Leckrone, D. S. 1998, *ApJ*, 500, 000
 Bray, R. J., Cram, L. E., Durrant, C. J., & Loughhead, R. E. 1991, *Plasma Loops in the Solar Corona* (Cambridge: Cambridge Univ. Press)
 Brosius, J. W., Davila, J. M., Thomas, R. J., & White, S. M. 1997, *ApJ*, 488, 488
 Chang, E. S., & Deming, D. 1995, in *IR Tools for Solar Astrophysics: What's Next?*, ed. J. R. Kuhn & M. J. Penn (Singapore: World Scientific), 47
 Collins, P. D. B. 1964, *ApJ*, 140, 1206
 Cowan, R. D. 1981, *The Theory of Atomic Structure and Spectra* (Berkeley: Univ. of California Press), chap. 15
 Craig, I. J. D., & Brown, J. C. 1976, *A&A*, 49, 239
 Dere, K. P., Landi, E., Mason, H. E., Monsignori Fossi, B. C., & Young, P. R. 1997, *A&AS*, 125, 149
 Dere, K. P., & Mason, H. E. 1993, *Sol. Phys.*, 144, 217
 Edlén, B. 1943, *Zeitschrift für Astrophysik*, 22, 30
 Erdos, G., Balogh, A., & Kota, J. 1997, *Adv. Space Res.*, 19, 843
 Ferland, G. J. 1993, *ApJS*, 88, 49
 Feuchtgruber, H., et al. 1997, *ApJ*, 487, 962
 Fineschi, S., Hoover, R. B., Zukic, M., Kim, J., Walker, A. B. C., J., & Baker, P. C. 1993, *Proc. SPIE*, 1742, 423
 Flower, D. R., & Pineau des Forêts, G. 1973, *A&A*, 24, 181
 Forsyth, F. J., Balogh, A., Horbury, T. S., & Smith, E. J. 1997, *Adv. Space Res.*, 19, 839
 Gary, D. E., & Hurford, G. J. 1994, *ApJ*, 420, 903
 Gelfreikh, G. B. 1994, in *IAU Colloq. 144, Solar Coronal Structures*, ed. V. Rusin, P. Heinzel, & J.-C. Vial (Bratislava, Slovakia: IVEDA Publishing Co.), 21
 Gelfreikh, G. B., & Lubyshev, B. L. 1979, *Soviet Astr.-AJ*, 23, 316
 Ginzburg, V., & Zheleznyakov, V. V. 1961, *Soviet Astron.-AJ*, 5, 1
 Golub, L., & Pasachoff, J. M. 1997, *The Solar Corona* (Cambridge: Cambridge Univ. Press)
 Greenhouse, M. A., Feldman, U., Smith, H. A., Klapisch, M., Bhatia, A. K., & Bar-Shalom, A. 1993, *ApJS*, 88, 23
 Grevesse, N., & Anders, E. 1991, in *Solar Interior and Atmosphere*, ed. A. N. Cox, W. C. Livingston, & M. S. Matthews (Tucson: Univ. of Arizona Press), 1227
 Harvey, J. W. 1969, Ph.D. thesis, Univ. Colorado, Boulder
 Jefferies, J. T., Orrall, F. Q., & Zirker, J. B. 1971, *Sol. Phys.*, 16, 103
 Judge, P. G., Woods, T. N., Brekke, P., & Rottman, G. J. 1995, *ApJ*, 455, L85
 Kastner, S. O. 1993, *Sol. Phys.*, 143, 197
 Kaufman, V., & Sugar, J. 1986, *J. Phys. Chem. Ref. Data*, 15, 321
 Koutchmy, S. 1995, in *IR Tools for Solar Astrophysics: What's Next?*, ed. J. R. Kuhn & M. J. Penn (Singapore: World Scientific), 1
 Kuhn, J. R. 1995, in *IR Tools for Solar Astrophysics: What's Next?*, ed. J. R. Kuhn & M. J. Penn (Singapore: World Scientific), 89
 Kuhn, J. R., Penn, M. J., & Mann, I. 1996, *ApJ*, 456, L67
 Kundu, M. R., Schmahl, E. J., & Gerassimenko, M. 1980, *A&A*, 82, 265
 Landi Degl'Innocenti, E. 1998, *Nature*, 392, 256
 Landi Degl'Innocenti, E., Landi Degl'Innocenti, E., & Landolfi, M. 1996, in *Forum THEMIS*, ed. N. Mein & S. Sahal-Bréchet (Meudon, France: Observatoire de Meudon), 59
 Lang, J. 1994, *At. Data Nucl. Data Tables*, 57, 1
 Lang, K. R., & Willson, R. F. 1982, *ApJ*, 255, L111
 Leka, K. D., Canfield, R. C., McClymont, A. N., & van Driel-Gesztelyi, L. 1996, *ApJ*, 462, 547
 Low, B. C. 1994, *Phys. Plasmas*, 1, 1684
 Low, B. C., & Hundhausen, J. R. 1995, *ApJ*, 443, 818
 Low, B. C., & Lou, Y. Q. 1990, *ApJ*, 352, 343
 Münch, G. 1966, *ApJ*, 145, 237
 Münch, G., Neugebauer, G., & McCammon, D. 1966, *ApJ*, 149, 681
 Oliva, E., Salvati, M., Moorwood, A. F. M., & Marconi, A. 1994, *A&A*, 288, 457
 Olsen, K. H., Anderson, C. R., & Stewart, J. N. 1971, *Sol. Phys.*, 21, 360
 Pallavicini, R., Sakurai, T., & Vaiana, G. S. 1981, *A&A*, 98, 316
 Parker, E. N. 1988, *ApJ*, 330, 474
 Penn, M. J., Arnaud, J., Mickey, D. L., & Labonte, B. J. 1994, *ApJ*, 436, 368
 Penn, M. J., & Kuhn, J. R. 1994, *ApJ*, 434, 807
 Pryce, M. H. L. 1964, *ApJ*, 140, 1192
 Raymond, J. C., & Doyle, J. G. 1981, *ApJ*, 247, 686
 Röhrlich, R., & Pecker, C. 1963, *ApJ*, 138, 1246
 Sahal-Bréchet, S. 1974, *A&A*, 36, 355
 ———. 1977, *ApJ*, 213, 887
 Schmelz, J. T., Holman, G. D., Brosius, J. W., & Willson, R. F. 1994, *ApJ*, 434, 786
 Schmieder, B., Demoulin, P., Aulanier, G., & Golub, L. 1996, *ApJ*, 467, 881
 Shibasaki, K., Chiuderi-Drago, F., Melozzi, M., Slottje, C., & Antonucci, E. 1983, *Sol. Phys.*, 89, 307
 Webb, D. F., Davis, J. M., Kundu, M. R., & Velusamy, T. 1983, *Sol. Phys.*, 85, 267
 White, S. M., Kundu, M. R., & Gopalswamy, N. 1991, *ApJ*, 366, L43
 Willson, R. F. 1985, *ApJ*, 298, 911